

# Spectral Characteristics and Photosensitization of TiO<sub>2</sub> Nanoparticles in Reverse Micelles by Perylenes

Laura I. Hernández,<sup>†</sup> Robert Godin,<sup>‡</sup> Jesse J. Bergkamp,<sup>§</sup> Manuel J. Llansola Portolés,<sup>§</sup> Benjamin D. Sherman,<sup>§</sup> John Tomlin,<sup>§</sup> Gerdenis Kodis,<sup>§</sup> Dalvin D. Méndez-Hernández,<sup>§</sup> Sonia Bertolotti,<sup>†</sup> Carlos A. Chesta,<sup>†</sup> Ernesto Mariño-Ochoa,<sup>||</sup> Ana L. Moore,<sup>§</sup> Thomas A. Moore,<sup>§</sup> Gonzalo Cosa,<sup>‡</sup> and Rodrigo E. Palacios<sup>\*,†</sup>

<sup>†</sup>Departamento de Química, Facultad de Ciencias Exactas Físico-Químicas y Naturales, Universidad Nacional de Río Cuarto, Río Cuarto, Córdoba S800, Argentina

<sup>‡</sup>Department of Chemistry and Center for Self Assembled Chemical Structures (CSACS/CRMAA), McGill University, Otto Maass Chemistry Building, 801 Sherbrooke Street West, Montreal, QC, H3A 0B8, Canada

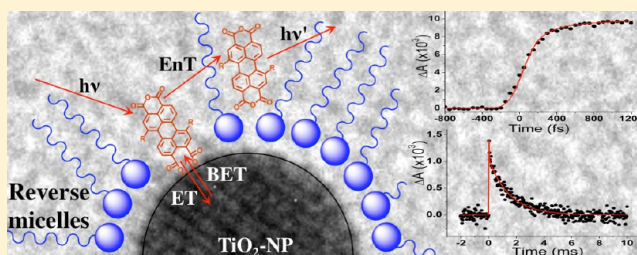
<sup>§</sup>Department of Chemistry and Biochemistry, Center for Bioenergy and Photosynthesis, Arizona State University, Tempe, Arizona 85287-1604, United States

<sup>||</sup>Department of Chemistry, Tecnológico de Monterrey, Campus Monterrey, Monterrey, NL, 64849, México

## Supporting Information

**ABSTRACT:** We report on the photosensitization of titanium dioxide nanoparticles (TiO<sub>2</sub> NPs) synthesized inside AOT (bis(2-ethylhexyl) sulfosuccinate sodium salt) reverse micelles following photoexcitation of perylene derivatives with dicarboxylate anchoring groups. The dyes, 1,7-dibromoperylene-3,4,9,10-tetracarboxy dianhydride (**1**), 1,7-dipyrrolidinylperylene-3,4,9,10-tetracarboxy dianhydride (**2**), and 1,7-bis(4-*tert*-butylphenoxy)perylene-3,4,9,10-tetracarboxy dianhydride (**3**), have considerably different driving forces for photoinduced electron injection into the TiO<sub>2</sub> conduction band, as estimated by electrochemical measurements and

quantum mechanical calculations. Fluorescence anisotropy measurements indicate that dyes **1** and **2** are preferentially solubilized in the micellar structure, creating a relatively large local concentration that favors the attachment of the dye to the TiO<sub>2</sub> surface. The binding process was followed by monitoring the hypsochromic shift of the dye absorption spectra over time for **1** and **2**. Photoinduced electron transfer from the singlet excited state of **1** and **2** to the TiO<sub>2</sub> conduction band (CB) is indicated by emission quenching of the TiO<sub>2</sub>-bound form of the dyes and confirmed by transient absorption measurements of the radical cation of the dyes and free carriers (injected electrons) in the TiO<sub>2</sub> semiconductor. Steady state and transient spectroscopy indicate that dye **3** does not bind to the TiO<sub>2</sub> NPs and does not photosensitize the semiconductor. This observation was rationalized as a consequence of the bulky *t*-butylphenoxy groups which create a strong steric impediment for deep access of the dye within the micelle structure to reach the semiconductor oxide surface.



## INTRODUCTION

The study of interfacial electron transfer (IET) in dye–semiconductor nanoparticle systems is an area of considerable research interest from both fundamental and practical points of view.<sup>1–6</sup> Modification of metal oxide semiconductors with organic dyes is a well-known method to extend their photoresponse to visible light. Application of metal oxide/dye systems has been extensively demonstrated in a variety of organic–electronic devices such as dye-sensitized solar cells (DSSC),<sup>7–12</sup> heterogeneous photocatalysis,<sup>13–18</sup> and chemical sensing.<sup>19–23</sup> The current need for performance improvement in many of these devices entails a better understanding of the IET process which plays a central role in device operation.<sup>1,12,24–27</sup>

Dye to semiconductor nanoparticle (NP) photoinduced electron transfer has been widely studied in nanostructured metal oxide semiconductor films where the dye molecules are deposited in a relatively uncontrolled manner leading to a number of physically adsorbed and nonbound aggregated dyes with poor electronic coupling with the semiconductor.<sup>28</sup> A large number of the electron transfer studies on these systems have been performed using steady state and time-resolved UV–vis spectroscopic techniques. The results obtained usually show

**Special Issue:** Paul F. Barbara Memorial Issue

**Received:** August 31, 2012

**Revised:** November 13, 2012

**Published:** November 28, 2012

complex kinetics and spectra due to the heterogeneous nature of the dye–NP binding, the size and crystallinity of the semiconductor NPs, scattering effects of the nanostructured film, and the presence of unbound trapped dye and dye aggregates.<sup>1,29–32</sup> The use of well characterized dye-sensitized NP suspensions can help to overcome many of these difficulties (by reducing scattering effects and providing a more homogeneous set of semiconductor NPs), and accordingly a large number of studies have been carried out on such systems.<sup>1,4–6,25,33–63</sup> In some of these studies, well dispersed and homogeneous semiconductor particle suspensions were obtained via a microemulsion method.<sup>39,52,53,56,58</sup>

Perylene based dyes have been extensively explored as photosensitizers for DSSC because they absorb strongly in the visible, are chemically photostable, and are amenable for fine-tuning their light absorbing and redox properties through structural modifications.<sup>64–75</sup> Additionally, the relatively low number of excited state relaxation pathways in perylenes, as compared to the prototypical ruthenium based dyes, facilitates the study of IET.<sup>75</sup> Binding of perylene derivatives to TiO<sub>2</sub> has been achieved through carboxylic acid and dicarboxylic acid groups derived from anhydrides.<sup>66–74</sup> The nature of the binding and the electronic coupling between the dye and the semiconductor has been shown to influence the dye excited state properties and IET behavior.<sup>66,67,69,73,74,76</sup> Binding of perylene derivatives to metal NPs and metal-oxide and nanorods has also been achieved through thiol and sulfide groups, respectively.<sup>77–79</sup>

Herein we report studies of the sensitization of TiO<sub>2</sub> nanoparticles in a reverse micelle suspension by perylene dye derivatives. The perylene dyes used in this study, (1,7-dibromoperylene-3,4,9,10-tetracarboxy dianhydride (1), 1,7-dipyrrolidinylperylene-3,4,9,10-tetracarboxy dianhydride (2), and 1,7-bis(4-*tert*-butylphenoxy)perylene-3,4,9,10-tetracarboxy dianhydride (3), contain cyclic anhydride moieties which hydrolyze to yield two carboxylic acid groups that serve as anchoring groups to the TiO<sub>2</sub> surface. Steady state and transient spectroscopic results indicate that a large portion of dyes 1 and 2 are attached to the TiO<sub>2</sub> NP surface and can effectively initiate IET. On the other hand, spectroscopic results show inefficient binding of dye 3 to the semiconductor surface and lack of photoinduced electron transfer, indicating that the bulky structure of the dye hampers the binding process within the micelle–TiO<sub>2</sub> NP structure.

## ■ EXPERIMENTAL AND THEORETICAL METHODS

**Materials.** Titanium tetraisopropoxide (TTIP, ≥97.0%), isopropanol (anhydrous, 99.5%), 3,4,9,10-perylenetetracarboxylic dianhydride (97%), 2,6-diisopropylaniline (97%), pyrrolidine (99%), and bis(2-ethylhexyl) sulfosuccinate sodium salt (AOT, 98%) were purchased from Sigma-Aldrich and used as received. Anhydrous *tert*-butyl alcohol was purchased from Alfa-Aesar and used as received. Thin layer chromatography plates (250 μm), with fluorescent and nonfluorescent indicators, were purchased from Analtech, Inc. Silica gel (SiliaFlash F60 40–63 μm) used for column chromatography was purchased from SILICYCLE. Syringe PTFE membrane (200 nm pore) filters: disposable assemblies (PALL, Acrodisc. CR 25 mm) and disposable membranes (Microclar, T02013WPH) on a reusable filter holder (Cole-Palmer, CZ-02928-10) were used interchangeably. *N*-Heptane (HPLC grade), ethanol (anhydrous, HPLC grade), and potassium hydroxide (KOH, ACS reagent grade) were purchased from Merk. Perchloric acid (ACS

reagent grade) was purchased from Taurus. Ultrapure water (18Ω, Millipore) and bottled water (Sintorgan, HPLC grade) were used interchangeably. Tetrahydrofuran (THF) (Sintorgan, HPLC) was distilled over metallic sodium with benzophenone. All solvents used for column chromatography were distilled before use.

**Synthesis.** 1,7-Dibromoperylene-3,4,9,10-tetracarboxy Dianhydride (1). Compound 1 was obtained following a literature procedure.<sup>74</sup>

1,7-Dipyrrolidinylperylene-3,4,9,10-tetracarboxy Dianhydride (2). Compound 2 was prepared following slightly modified reported protocols. First, *N,N'*-bis(2,6-diisopropylphenyl)-1,7-bis(pyrrolidin-1-yl)perylene-3,4,9,10-tetracarboxylic acid bisimide was prepared.<sup>74</sup> This was followed by base hydrolysis in *tert*-butyl alcohol and purification by column chromatography using 2% ethyl acetate in chloroform as eluent on silica gel<sup>80</sup> to yield compound 2. All compounds were characterized by <sup>1</sup>H NMR and MALDI-TOF mass spectrometry; the spectra were identical to those previously reported.

1,7-Bis(4-*tert*-butylphenoxy)perylene-3,4,9,10-tetracarboxy Dianhydride (3). Compound 3 was prepared following a modified published procedure.<sup>81</sup> A portion of compound 1 (8 g, 14.5 mmol), 4-*tert*-butylphenol (7.2 g, 48.0 mmol), and cesium carbonate (9.5 g, 29.1 mmol) were dissolved in dimethylformamide (485 mL) and heated at reflux for 4 h under nitrogen. The reaction mixture was poured into water (200 mL) and neutralized with aqueous 1 M HCl. The precipitate was filtered and washed repeatedly with water and then methanol to give a crude solid. A 100 mg portion was then purified by preparatory TLC, which was followed by flash column chromatography on silica gel using chloroform as the eluent to afford a red solid (15.4 mg, 0.022 mmol, 15.4% yield). <sup>1</sup>H NMR (Chloroform-*d*, 400 MHz): δ<sub>H</sub>, ppm 9.64 (d, *J* = 8.2 Hz, 2 H), 8.71 (d, *J* = 8.2 Hz, 2 H), 8.28 (s, 2 H), 7.52 (d, *J* = 8.6 Hz, 4 H), 7.13 (d, *J* = 8.6 Hz, 4 H), 1.39 (s, 18 H).

**Titanium Dioxide Nanoparticles (TiO<sub>2</sub> NPs).** The synthesis was carried out by the hydrolysis of TTIP inside the water pool of AOT reverse micelles suspended in *n*-heptane.<sup>52</sup> In this system, the micelles act as nanoreactors, where the hydrolysis reaction takes place, preventing the formation of TiO<sub>2</sub> nanoparticle aggregates. A micellar suspension of *w*<sub>0</sub> = 1 (*w*<sub>0</sub> = [H<sub>2</sub>O]/[AOT]) was prepared by adding 220 μL of aqueous HClO<sub>4</sub> (0.02 M) to 30 mL of AOT solution (0.4 M) in *n*-heptane under continuous stirring. A 0.2 mL aliquot of a TTIP stock solution (0.136 M) in anhydrous isopropanol was added dropwise to 30 mL of the micellar suspension under mild agitation at room temperature. Stirring was continued for 20 min to obtain a clear micellar suspension containing TiO<sub>2</sub> NPs (see Figure 2, inset).

**Micelles without TiO<sub>2</sub> NPs.** A control sample of micelles without TiO<sub>2</sub> NPs was prepared following exactly the same procedure described above except for the addition of TTIP. We estimate a significant proton concentration inside the reverse micelle water pool based on the concentration of HClO<sub>4</sub> in the aqueous solution used for micelle formation. However, calculation of pH is not valid in these systems where the nanoscopic size of the water pool limits the number of available water molecules.<sup>82</sup>

**Instruments and Measurements.** *Steady State Absorption.* Spectra were recorded in 1 cm path length cuvettes with the following spectrophotometers: diode array HP 8452, Shimadzu - UV-IR (2041PC), and Hitachi double beam UV/vis spectrophotometer (U-2800).

**Steady State Fluorescence.** Spectra and fluorescence anisotropy measurements were obtained with the following spectrofluorometers: Horiba FluoroMax-4 and PTI Quanta-master 40, both equipped with motorized polarizers. To compare emission intensities of samples measured with absorbances not matched at the excitation wavelength ( $\text{Abs}(\lambda_{\text{ex}})$ ), the corrected emission intensity of a given sample ( $I_{\text{corr}}(\lambda_{\text{em}})$ ) was calculated from the observed emission intensity ( $I_{\text{obs}}(\lambda_{\text{em}})$ ) using eqs 1 and 2:<sup>83</sup>

$$I_{\text{A,corr}}(\lambda_{\text{em}}) = \left( \frac{\text{Abs}_{\text{B}}(\lambda_{\text{ex}})}{\text{Abs}_{\text{A}}(\lambda_{\text{ex}})} \right) I_{\text{A,obs}}(\lambda_{\text{em}}) 10^{((\text{Abs}_{\text{A}}(\lambda_{\text{ex}}) + \text{Abs}_{\text{B}}(\lambda_{\text{em}}))/2)} \quad (1)$$

and

$$I_{\text{B,corr}}(\lambda_{\text{em}}) = I_{\text{B,obs}}(\lambda_{\text{em}}) 10^{((\text{Abs}_{\text{B}}(\lambda_{\text{ex}}) + \text{Abs}_{\text{B}}(\lambda_{\text{em}}))/2)} \quad (2)$$

where  $\lambda_{\text{ex}}$  and  $\lambda_{\text{em}}$  are excitation and emission wavelengths, respectively, and the subscripts A and B correspond to the different samples for which the emission intensity is compared.

**Time Resolved Fluorescence.** Fluorescence lifetime measurements were performed with a time-correlated single photon counting (TC-SPC) system. The excitation source was a fiber supercontinuum laser based on a passive mode-locked fiber laser and a high-nonlinearity photonic crystal fiber supercontinuum generator (Fianium SC450). The laser provides 6 ps pulses at a repetition rate variable between 0.1 and 40 MHz. The laser output was sent through an Acousto-Optical Tunable Filter (Fianium AOTF) to obtain excitation pulses at the desired wavelength. Fluorescence emission was collected at 90° and detected using a double-grating monochromator (Jobin-Yvon, Gemini-180) and a microchannel plate photomultiplier tube (Hamamatsu R3809U-50). The polarization of the emission was 54.7° relative to that of the excitation. Data acquisition was done using a single photon counting card (Becker-Hickl, SPC-830). The IRF had a FWHM of ~50 ps, measured from the scattering of sample at the excitation wavelength. The data was globally fitted as a sum of exponential decays including IRF deconvolution using locally written software (ASUFIT)<sup>84</sup> developed in a MATLAB environment (Mathworks Inc.).

**Time Resolved Absorption.** Femtosecond to nanosecond transient absorption measurements were acquired with a kilohertz pulsed laser source and a pump–probe optical setup. Laser pulses of 100 fs at 800 nm were generated from an amplified, mode-locked titanium sapphire kilohertz laser system (Millennia/Tsunami/Spitfire, Spectra Physics). Part of the laser pulse energy was sent through an optical delay line and focused onto a 2 mm sapphire plate to generate a white light continuum for probe beam. The remainder of the pulse energy was used to pump an optical parametric amplifier (Spectra Physics) to generate excitation pulses at different wavelengths, which were modulated using a mechanical chopper. The excitation intensity was adjusted using a continuously variable neutral density filter. The probe beam was sent through a monochromator (SP150, Action Res. Corp.) and recorded by a diode detector (model 2032, New Focus Inc.) and boxcar (SR250, Stanford Research Systems). The instrument response function was ca. 200 fs.

Nanosecond transient absorption measurements were recorded with excitation from an optical parametric oscillator pumped by the third harmonic of a Nd:YAG laser (Ekspla NT342B). The pulse width was ~4–5 ns, and the repetition

rate was 10 Hz. The detection portion of the spectrometer (Proteus) was manufactured by Ultrafast Systems. The instrument response function was ca. 4.8 ns.

Transient absorption data analysis was carried out using ASUFIT. In brief, decay-associated spectra were obtained by fitting the transient absorption kinetic traces over a selected wavelength region simultaneously as described by eq 3 (parallel kinetic model)

$$\Delta A(\lambda, t) = \sum_{i=1}^n A_i(\lambda) \exp(-t/\tau_i) \quad (3)$$

where  $\Delta A(\lambda, t)$  is the observed absorption change at a given wavelength at time delay  $t$  and  $n$  is the number of kinetic components used in the fitting. A plot of  $A_i(\lambda)$  versus wavelength is called a decay-associated spectrum (DAS), and represents the amplitude spectrum of the  $i$ th kinetic component, which has a lifetime of  $\tau_i$ . The global analysis procedures described here have been extensively reviewed. Random errors associated with the reported lifetimes obtained from fluorescence and transient absorption measurements were typically  $\leq 5\%$ .

**Structural Characterization.** <sup>1</sup>H NMR spectra were recorded on a 400 MHz Varian Liquid-State spectrometer. NMR samples were dissolved in deuteriochloroform with 0.03% tetramethylsilane as an internal reference. Mass spectra were obtained on an Applied Biosystems Voyager-DE STR matrix-assisted laser desorption/ionization time-of-flight spectrometer (MALDI-TOF).

**Dynamic Light Scattering (DLS).** Measurements were performed with a Malvern Instrument 4700 system with detection at 90° from the excitation, at a temperature of 25 °C, and using the 488 nm spectral line of an argon ion laser. Light scattering results were analyzed with Zetasizer software (provided by the manufacturer) to obtain hydrodynamic radius distributions and polydispersity indexes. Microemulsion solutions were filtered through 200 nm pore filters right before data acquisition. Extreme care was taken to reduce the contamination by dust.

**Electrochemical Measurements.** Cyclic voltammograms on **1**, **2**, and **3** in solution were carried out in benzonitrile (**1**) or acetonitrile (**2**, **3**) with 100 mM tetrabutylammonium hexafluorophosphate as supporting electrolyte. A three electrode setup, consisting of a glassy carbon disc working electrode, platinum gauze counter electrode, and Ag<sup>+</sup>/Ag quasireference, was used with the sample volume under an argon atmosphere. A CH Instruments 760D potentiostat and corresponding software were used for all measurements. The Ag<sup>+</sup>/Ag quasireference was calibrated to the ferrocenium/ferrocene (Fc<sup>+</sup>/Fc) couple with  $E_{\text{Fc}^+/\text{Fc}}$  taken as 0.45 V vs saturated calomel electrode (SCE).

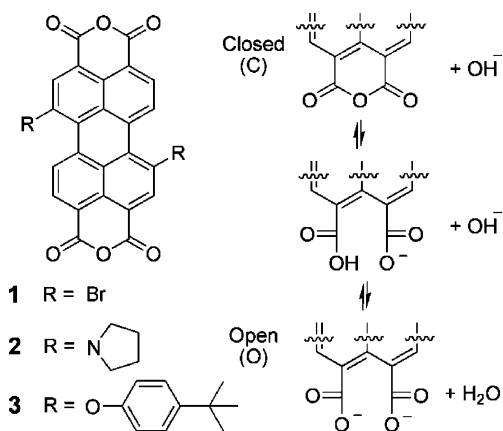
**Transmission Electron Microscopy.** TEM micrographs were collected using a Philips CM200 TEM at 200 kV. The TiO<sub>2</sub>–micelle microemulsion was plated on a plasma treated (10 min, air intake) 200-mesh carbon coated copper grid (Canemco, Lakefield, QC, Canada) for 1 min before wicking using filter paper. The grid was then rinsed with high purity water (HyClone, Logan, UT) to wash AOT surfactant away. TEM micrographs were analyzed using ImageJ software.<sup>85</sup> The “analyze particle” plug-in was used to find the outline and calculate the diameter of nanoparticles on arbitrarily thresholded images.

**Computational Methodology.** Geometry optimizations of dyes 1, 2, and 3 (in their open (O) and closed (C) forms) (see Figure S3a in the Supporting Information) were performed with Gaussian 09<sup>86</sup> using density functional theory (DFT) calculations at the B3LYP/6-31G(d) level of theory.<sup>87–94</sup> Using the conductor-like polarizable continuum model (CPCM), acetonitrile was implicitly included for all the optimizations.<sup>95,96</sup>

## RESULTS AND DISCUSSION

**Perylene Dyes. Molecular Structure.** The structures of perylene derivatives 1, 2, and 3 are shown in Scheme 1. On the

**Scheme 1. (left) Molecular Structure of Dyes 1, 2, and 3; (right) Opening of Anhydride Ring under Basic Catalysis**



basis of the structure of the dyes, at least three species in equilibrium can be proposed during the hydrolysis of an anhydride group (catalyzed in basic media), as shown in Scheme 1 (right). Partially hydrolyzed and/or deprotonated species, i.e., involving only one of the two anhydride rings present in the dyes, were not considered in this scheme but are also possible. As it is discussed below, the opening of at least one anhydride group to yield a dicarboxylic acid species is necessary for binding of the dyes to the TiO<sub>2</sub> surface. The precise nature of the interaction between the carboxylic group and the TiO<sub>2</sub> surface atoms still remains a subject of debate. Possible binding modes of the carboxylic acid species to the TiO<sub>2</sub> surface involve bidentate simple adsorption (electrostatic attraction and hydrogen bonding) and chemical bonding (ester linkage, bridging, and chelating).<sup>76,97</sup>

**Spectroscopic Characterization in Homogeneous Solution.** Figure 1 shows the absorption and fluorescence of dyes 1 and 2 in ethanol ( $\sim 10^{-6}$  M) as a function of time and addition of base (potassium hydroxide). The solutions were prepared by addition of a small aliquot (100  $\mu$ L) of dye stock solution in THF (in this solvent, the dyes are present in the anhydride form, species C, Scheme 1) to 3 mL of ethanol with continuous stirring. The acquisition of spectra as a function of time started immediately after the stock dye solution was added to ethanol. For perylenes 1 and 3, both absorption and fluorescence spectra (Figure 1a and b) show clear isosbestic and isoemissive points, indicating the interconversion between two species with distinct spectra and similar fluorescence quantum yields. The species that absorb and emit at longer wavelengths are assigned to the anhydride form (C, Scheme 1), while the shorter wavelength absorption and emission spectra are assigned to the

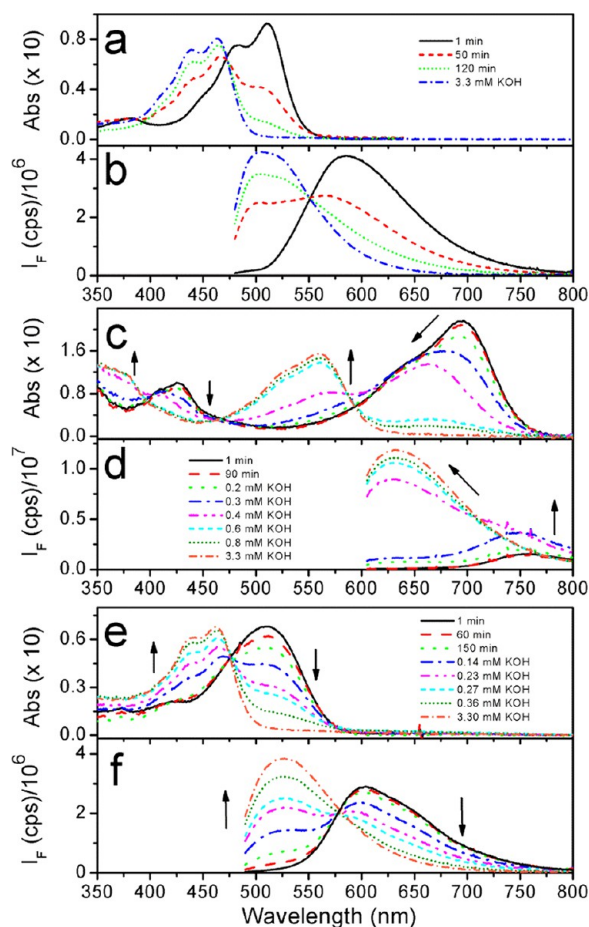


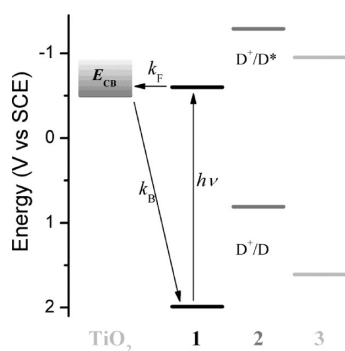
**Figure 1.** Absorption and emission spectra of 1 (a, b), 2 (c, d), and 3 (e, f) in ethanol as a function of time and KOH addition. Emission spectra for 1 and 3 were taken with excitation at the isosbestic point (472 and 475 nm, respectively). Emission spectra for 2 were taken with excitation at 594 nm. The dye concentration was  $\sim 10^{-6}$  M for all samples. Arrows indicate the direction of change.

fully hydrolyzed form for each dye (O, Scheme 1).<sup>66,67,69–71</sup> In the case of 2, isosbestic points and isoemissive points were not observed. This indicates that there are more than two interconverting species with significantly different spectra, presumably protonated/deprotonated amines, protonated/deprotonated carboxylic acids, or zwitterionic species. For all perylenes, the spectral changes observed indicate that the addition of a strong base (potassium hydroxide) is necessary to shift the equilibrium between the anhydride species (C, Scheme 1) and its hydrolyzed form (O, Scheme 1) toward the later. The base catalyzes the hydrolysis of the cyclic anhydride and deprotonates the resulting dicarboxylic acid (species O, Scheme 1). Figure 1a, c, and e show that the absorption spectra of the freshly prepared ethanol solutions (where the anhydride species prevails) are significantly bathochromically shifted (49, 134, and 48 nm for 1, 2, and 3, respectively) compared to the corresponding spectra after base addition (when the fully hydrolyzed species prevails). The fluorescence spectra shown in Figure 1a and c were recorded with excitation at the isosbestic point for 1 and 3 (472 and 478 nm, respectively) to allow for the direct comparison of the relative fluorescence quantum yields of the anhydride and hydrolyzed species. The resulting fluorescence intensities indicate that the emission quantum yields ( $\Phi_F$ ) of both species (C and O) are very similar for these

perylene. For **2** the emission spectra were corrected for the number of photons absorbed at the excitation wavelength as described in the experimental section. Comparison of emission intensities before and after base addition for **2** (Figure 1d) indicates that the emission quantum yield of the hydrolyzed form is significantly larger than that of the dianhydride form ( $\Phi_F^O > 8 \Phi_F^C$ ). The spectral changes observed upon hydrolysis of the dyes in solution are consistent with previous reports on analogous dyes<sup>66,67,69,70,74</sup> and were useful for monitoring the kinetics of dye binding to TiO<sub>2</sub> as described below.

**Energy Diagram.** Scheme 2 shows the relative energetics for the oxidation of the ground and excited states of the dyes and

**Scheme 2. Diagram Depicting the Potentials for the First Oxidation and for the Oxidation of the Optically Excited States of 1, 2, and 3 and the TiO<sub>2</sub> Conduction Band (CB) Energy<sup>a</sup>**



<sup>a</sup>D/D<sup>+</sup> values were measured electrochemically for the anhydride (closed) form of the dye. D/D\* values were calculated as described in the text from the  $E_{00}$  energy of the hydrolyzed (open) form of the dyes.

the conduction band edge ( $E_{CB}$ ) of TiO<sub>2</sub>. The potential for the first oxidation (D<sup>+</sup>/D) of the dyes was measured electrochemically for the cyclic anhydride (closed) form of the dyes. Attempts to measure D<sup>+</sup>/D of the hydrolyzed (open) form were unsuccessful; thus, to a first approximation, the D<sup>+</sup>/D of the C form will be used for calculations through the text. The potential for the oxidation of the excited state (D<sup>+</sup>/D\*) was calculated with the equation  $D^+/D^* = D^+/D - E_{00}$ , where  $E_{00}$  is the zero-zero optical excitation energy estimated from the intersection of the normalized absorption and emission spectra of the hydrolyzed (open) species in ethanol (see Figure S1 in the Supporting Information). The  $E_{CB}$  value of TiO<sub>2</sub> was estimated as the flat-band potential<sup>98</sup> of polycrystalline TiO<sub>2</sub>, -0.52 vs SCE at pH 2,<sup>99</sup> to account for the concentration of

protons in the micelle water before NP formation. On the basis of energetic considerations, according to Scheme 2, all the dyes are capable of photoinjecting an electron in the conduction band of TiO<sub>2</sub>. Two additional factors not considered in Scheme 2 could in principle lead to a higher driving force for the photoinduced IET process: (a) the oxidation potentials of similar dyes attached to the TiO<sub>2</sub> surface in their open bound form are known to shift anodically relative to those in solution in their closed form<sup>67,69,71</sup> and (b) the presence of trap-sites energetically situated between the valence and conduction bands of the TiO<sub>2</sub> NPs which could act as electron acceptors. Finally, the size-quantization effect observed in the TiO<sub>2</sub> NPs used herein (*vide infra*) could lead to a negative shift of  $E_{CB}$  shown in Scheme 2, resulting in a decreased driving force for photoinduced electron transfer. Since the magnitude of the factors mentioned before cannot be estimated accurately, Scheme 2 provides only a first approximation for the energetics of the system.

Quantum mechanical calculations were performed to correlate molecular structure with the experimental electrochemical and spectroscopic parameters. The calculated HOMO–LUMO energies and energy gaps are summarized in Table 1. Rationalizing the DFT calculations by means of molecular orbital analysis, it was observed that both the HOMO and LUMO energies of all dyes shifted to less negative energies (vs vacuum) upon opening of the anhydride ring. Also, the HOMO–LUMO gap of all dyes increased upon opening of the anhydride with respect to the closed form, resulting in a hypsochromic shift of the absorption spectra. These two observations combined yield an increase in the driving force for photoinduced injection. These results are in agreement with previous work on analogous perylenes<sup>65,66,70,71</sup> and correlate well with the electrochemical and spectroscopic data presented in Table 1 and Figure 1.

**Titanium Dioxide Nanoparticles (TiO<sub>2</sub> NPs). Characterization.** The hydrodynamic diameter distribution of the micellar suspension before and after the addition of TTIP stock was measured by DLS. As shown in Figure 2a (gray bars), the mean hydrodynamic diameter ( $d$ ) of the micelles before TTIP addition was found to be  $d = 3.8 \pm 0.5$  nm (mean and standard deviation of three independent experiments). After formation of TiO<sub>2</sub> NPs, the mean hydrodynamic diameter of the micelle/TiO<sub>2</sub> microemulsion is slightly increased to  $d = 4.5 \pm 0.1$  nm; see Figure 2a (black bars). As seen in this figure, the size distribution of the micelle microemulsion with TiO<sub>2</sub> NPs is narrower than that of the micelles without TiO<sub>2</sub> NPs. This effect can be attributed to the fact that micelles without TiO<sub>2</sub> inside are inherently dynamic systems continually exchanging

**Table 1. Energetics of 1, 2, and 3 Estimated by Electrochemistry, Spectroscopy, and Quantum Mechanical Calculations**

	Ox(1) <sup>a</sup>	Ox(2) <sup>a</sup>	Red(1) <sup>a</sup>	Red(2) <sup>a</sup>	HOMO <sup>b</sup>	LUMO <sup>b</sup>	HOMO–LUMO gap <sup>b</sup>	$E_{00}$ <sup>c</sup>
1-C	1.99 (irr)		-0.25 (61)	-0.52 (64)	1.99	-0.52	2.51	2.32
1-O					1.83	-0.82	2.65	2.59
2-C	0.81 (47)	0.91 (35)	-0.72 (61)		0.86	-1.08	1.94	1.71
2-O					0.73	-1.40	2.13	2.10
3-C	1.61 (65)		-0.51 (52)	-0.70 (55)	1.56	-0.80	2.36	2.22
3-O					1.41	-1.10	2.51	2.56

<sup>a</sup> $E_{1/2}$  values for the indicated process reported in V vs SCE with the peak separation ( $\Delta E_p$ ) given in mV. <sup>b</sup>Calculated HOMO and LUMO energies (see Figure S3a in the Supporting Information) were normalized to the experimental oxidation potential of 1-C vs SCE by the equation  $E_{vs\ SCE} = -E_{cal} - 4.26$  eV. <sup>c</sup>Determined from the intersection of the normalized emission and absorption spectra (measured in ethanol, Figure 1S in the Supporting Information) with the equation  $E_{00}$  (eV) =  $1240/\lambda$  (nm).

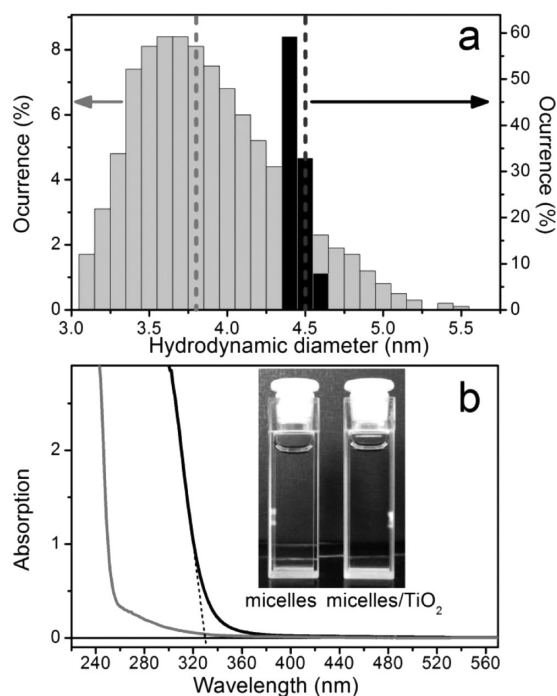


**Figure 2.** (a) DLS measurements of microemulsions without (gray bars) and with (black bars)  $\text{TiO}_2$  NPs. Dashed lines indicate the corresponding mean diameter values for each sample. (b) Absorption spectra of microemulsions without (gray) and with (black)  $\text{TiO}_2$  NPs. The inset shows a photograph of the micelle and micelle- $\text{TiO}_2$  microemulsions.

water from the inner pool and surfactant molecules with other micelles, so that its size varies constantly. In the case of micelles containing  $\text{TiO}_2$  NPs, the surfactant movement is much more restricted, possibly due to attractive electrostatic interactions between the negatively charged polar head of the surfactant and the positively charged oxide surface under the acidic conditions inside the water pool. Estimation of the total concentration of micelles ( $C_m = 10^{-3}$  M) and of  $\text{TiO}_2$  NPs ( $C_{\text{NP}} = 10^{-6}$  M) (see details in the Supporting Information) in the resulting solution after NP formation indicates that a large fraction of the total micelles do not contain  $\text{TiO}_2$  NPs. Considering this estimation, we rationalize the significant difference observed for the DLS results of micelles with and without  $\text{TiO}_2$  NPs as a consequence of a higher light scattering efficiency of the  $\text{TiO}_2$  NP vs that of “empty” micelles.

Spectroscopic evidence for the formation of  $\text{TiO}_2$  particles is seen in the absorption spectra. Figure 2b shows the absorption spectra of micelles before (dashed line) and after the addition of TTIP (solid line). In the latter, the strong absorption in the UV region is assigned to the  $\text{TiO}_2$  band gap transition. It is well-known that the band gap of semiconductors is modulated by quantum confinement effects when the particle size reaches nanometric dimensions.<sup>100,101</sup> These size-induced quantum effects produce an increase of the band gap which results in a blue-shift of the optical absorption. However, some reports in the literature indicate unusual variation of the oscillator strength of the first allowed direct transition in  $\text{TiO}_2$  NPs (as a consequence of structural size effects) and caution about the use of the absorption shifts to estimate NP size based on quantization effects.<sup>102</sup> Other reports indicate that the presence of surface states and formation of a surface dipole layer on the surface of  $\text{TiO}_2$  NPs synthesized in inverse micelles leads to

sub-band gap absorption, making the comparison of shifts unreliable.<sup>103</sup> Our  $\text{TiO}_2$  NPs show a significant blue shift in the absorption spectra relative to that of bulk  $\text{TiO}_2$ . Assuming that this shift is due to quantum effects, the apparent band gap of the NPs can be estimated as  $E_{\text{BG}} \sim 3.88$  eV (see Figure S2 in the Supporting Information). This putative  $E_{\text{BG}}$  of  $\text{TiO}_2$  NPs is significantly higher than that of bulk  $\text{TiO}_2$  (3.2 and 3.0 eV for anatase and rutile phases, respectively), suggesting significant size-quantization.<sup>53,103–105</sup> The prepared micelle/ $\text{TiO}_2$  microemulsion has very low light scattering effects even at wavelengths below 350 nm due to the small average size of the  $\text{TiO}_2$  NP and narrow size distribution, being an ideal system for spectroscopic studies.

The morphology and crystallinity of the synthesized  $\text{TiO}_2$  NPs were studied by transmission electron microscopy (TEM). The micrographs in Figure 3 show nearly spherical particles

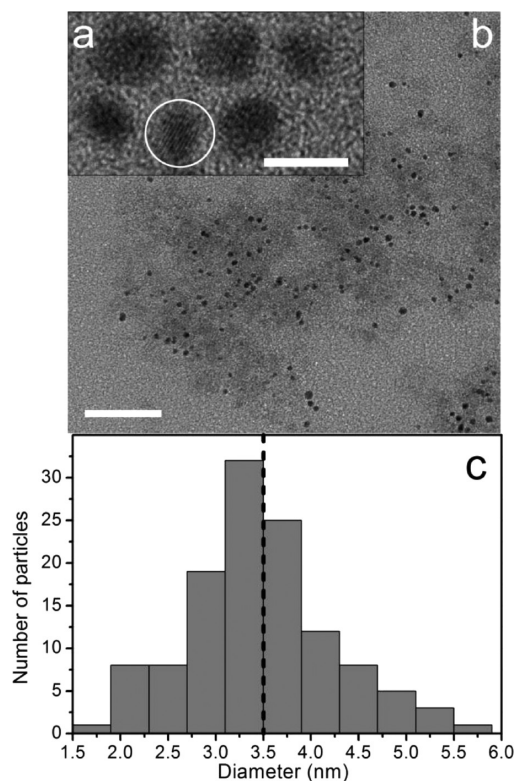


**Figure 3.** TEM micrographs of  $\text{TiO}_2$  nanoparticles synthesized in AOT reverse micelles. (a) High magnification image showing crystallinity in the circled  $\text{TiO}_2$  nanoparticle. Scale bar = 5 nm. (b) Representative region showing  $\text{TiO}_2$  nanoparticles as dark circles and excess AOT surfactant as dark gray areas. Scale bar = 50 nm. (c) Histogram of nanoparticle diameter constructed by analyzing TEM micrographs; see details in text. The dashed line indicates the mean diameter value.

with an estimated mean diameter of  $3.5 \pm 0.7$  nm (average from 123 particles). The particles have a relatively narrow size distribution, as shown on the histogram in Figure 3c. These measurements are consistent with the DLS results showing a mean diameter for the “naked”  $\text{TiO}_2$  NPs which is slightly smaller than the mean hydrodynamic diameter of the  $\text{TiO}_2$ -micelle system. High resolution TEM (HRTEM) images (Figure 3a) show, for some particles, clear crystal planes with an average spacing of  $2.186 \pm 0.004$  Å (mean from 6 NPs), which matches well the literature values of the (111) planes of

bulk rutile  $\text{TiO}_2$  (2.188 Å, (111) plane); no interplanar spacing in the anatase phase matches this value. Even though this information is not sufficient to categorically assign a crystal structure to the synthesized nanoparticles, since this would require a more detailed study involving diffraction experiments, the results suggest the rutile phase as the most likely one. However, given the large number of factors that affect the observation of NP crystalline structure in TEM micrographs,<sup>106</sup> we cannot make a definitive assignment of the crystalline nature of the prepared  $\text{TiO}_2$  nanoparticles based only on HRTEM images.

**Dye– $\text{TiO}_2$  NP Systems. Assembly.** Binding of perylene 1 and 2 to  $\text{TiO}_2$  NPs in a microemulsion was carried out by addition of 100  $\mu\text{L}$  of dye stock solution ( $\sim 10^{-4}$  M) in THF to 3 mL of a  $\text{TiO}_2$ –NP–micelle suspension ( $[\text{TiO}_2] = 0.109$  g/L) in *n*-heptane (for pump–probe experiments, the dye/ $\text{TiO}_2$  NP concentration ratio was increased 2 times). The microemulsion was left incubating for >4 h, and absorption spectra were recorded at periodic time intervals immediately after addition of the dye, as shown in Figure 4. A control sample of micelles without  $\text{TiO}_2$  was prepared as described in the Materials section and analyzed in an analogous manner. The hypsochromic shift observed in the absorption spectra of dyes 1 and 2 in the presence of  $\text{TiO}_2$  is indicative of opening of the anhydride ring and suggests binding of the resulting

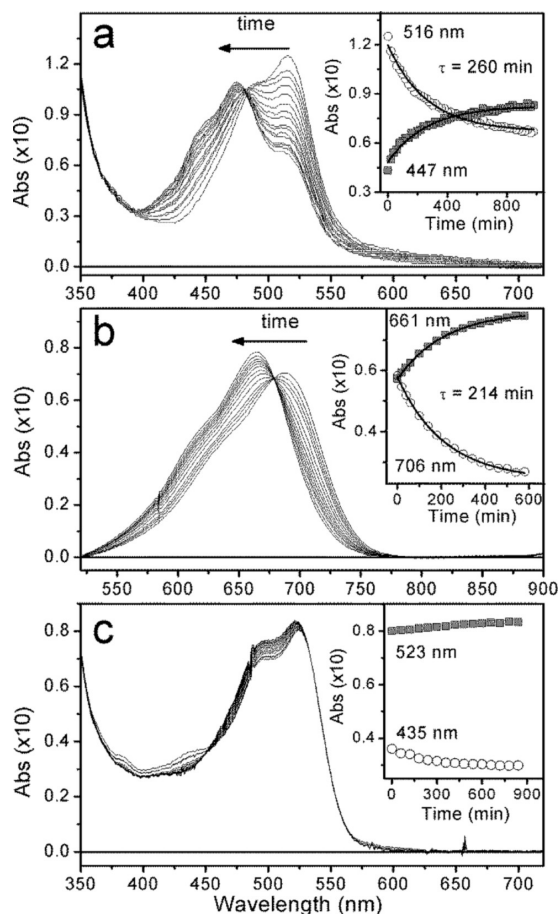


**Figure 4.** Absorption spectra of 1 (a), 2 (b), and 3 (c) in a microemulsion containing  $\text{TiO}_2$  NPs as a function of time. The inset displays kinetic traces at the indicated wavelengths (circles and squares) and corresponding monoexponential fittings (solid lines) with a shared time constant.

dicarboxylic form of the dye to the semiconductor.<sup>65–71,73,74</sup> Further evidence for dye binding to the oxide surface comes from time-resolved experiments that are described in detail below and which show the formation of the dye<sup>•+</sup>– $\text{TiO}_2$ (e<sup>−</sup>) charge separated state. Other authors have confirmed binding of dyes (containing carboxylic acid moieties) to  $\text{TiO}_2$  films using FTIR by monitoring the frequency shift of the carbonyl band upon acid deprotonation and binding to the oxide surface.<sup>107,108</sup> In the micelle systems described herein, AOT surfactant molecules are in an  $\sim 10^5$ -fold excess relative to dye molecules (*vide infra*); thus, the IR absorption of the AOT ester groups dominates the carbonyl band signal and precludes observation of dye binding to  $\text{TiO}_2$  by vibrational spectroscopy. In both systems, 1- $\text{TiO}_2$  and 2- $\text{TiO}_2$ , the binding of the dye was a relatively slow process, as shown by the kinetic traces in the insets of Figure 4a,b. When 3 was added to a  $\text{TiO}_2$  NP microemulsion, no significant changes were observed in the absorption and emission spectra over time, indicating that the dye's anhydride groups are not hydrolyzed. Under these conditions, the attachment of the dye to the  $\text{TiO}_2$  surface through the possible binding modes of the carboxylic acid species is precluded.

Figure 5 shows the absorption, fluorescence emission, and excitation spectra of the dyes in samples described above after incubation for 17 h. No further spectral changes were observed beyond this time. The absorption spectrum of 1 in the presence of  $\text{TiO}_2$  NPs (Figure 5a, solid line) shows clear contributions from two distinct species, referred to as 1-C and 1-OB (for closed-unbound and open-bound to  $\text{TiO}_2$ , respectively), with absorption peaks ( $\text{Abs}_{\text{max}}$ ) at  $\sim 519$  and 471 nm, respectively. The presence of the  $\text{TiO}_2$  NPs is confirmed by the strong absorption in the UV region (below 360 nm); see Figure 5a, solid and dotted lines. The corresponding fluorescence excitation spectrum (Figure 5a, dashed line) indicates that 1-C is the species that contributes predominantly to the observed fluorescence. The absorption and fluorescence excitation spectra of the control sample without  $\text{TiO}_2$  NPs (Figure 5b) show that 1-C is the only species present in the absence of  $\text{TiO}_2$  NPs. Note that in this case the strong  $\text{TiO}_2$  absorption in the UV region is not observed.

Analogous preparation and analysis using perylene 2 shows similar results (Figure 5c and d). In this case, the observed shift ( $\sim 25$  nm) is significantly smaller than that observed in ethanol upon full basic hydrolysis ( $\sim 134$  nm); this difference could be explained considering only partial hydrolysis of the dye in the  $\text{TiO}_2$ –micelle microemulsion. Thus, the spectra with peak absorption at  $\sim 690$  and 665 nm are assigned to the anhydride (closed, 2-C) and partially hydrolyzed (open bound, 2-OB, i.e., only one anhydride group is hydrolyzed) forms of 2, respectively. Evidence for the putative partial hydrolysis of 2 in ethanol is shown as a small shift in the absorption and emission spectra upon addition of a few equivalents of KOH; see Figure 1c (blue dash-dotted line). As mentioned before, the lack of an isosbestic point in Figure 1c suggests the presence of more than two interconverting species for 2.

The absorption and emission spectra of 3 did not show significant changes in  $\text{TiO}_2$ –micelle vs empty micelle microemulsions, as shown in Figure 5e and f. The lack of spectral shift and low emission quenching suggest that the dye does not open and bind to the oxide and consequently cannot effectively photoinject an electron in its conduction band. The deficient binding of the dye is rationalized as a consequence of the bulky 4-*tert*-butylphenoxy groups which create a strong steric

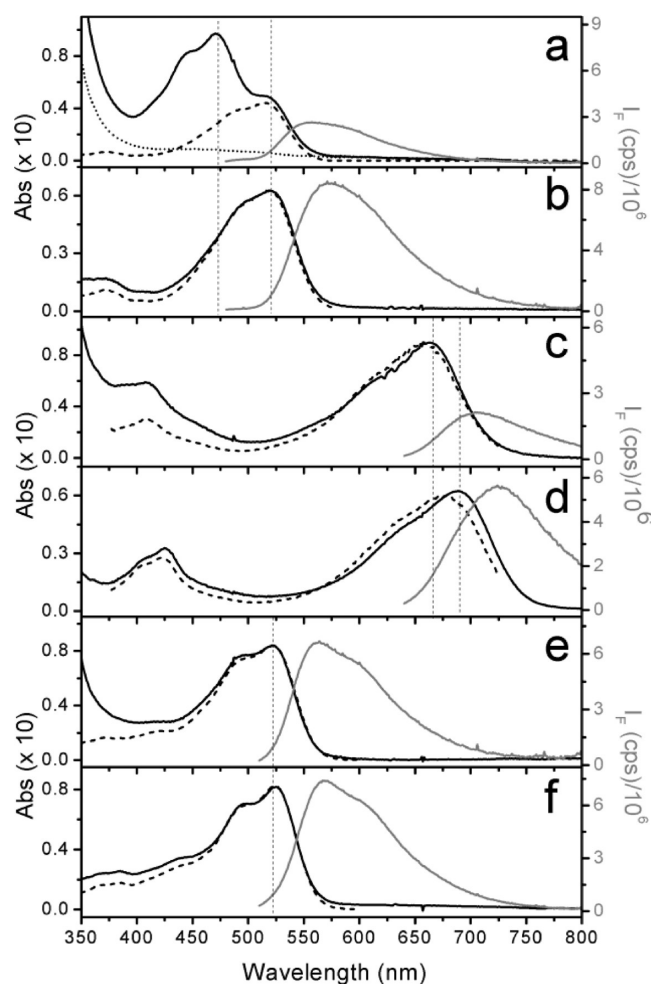


**Figure 5.** (a) Absorption (solid black), emission (solid gray), and normalized excitation spectra (dash) of perylene **1** in a microemulsion containing  $\text{TiO}_2$  NPs and absorption of a microemulsion containing  $\text{TiO}_2$  NPs (dotted line) but not the dye. (b) Same as part a but for a microemulsion without  $\text{TiO}_2$ . (c, d) Same as parts a and b, respectively, for perylene **2**. (e, f) Same as parts a and b for perylene **3**. Excitation spectra were recorded with emission at 578, 735, and 610 nm for (a, b), (c, d), and (e, f), respectively. Emission spectra were recorded with excitation at 470, 630, and 495 nm for (a, b), (c, d), and (e, f), respectively. Emission spectra intensities were corrected as described in the experimental section. Vertical dotted lines show absorption maximum in microemulsions with and without  $\text{TiO}_2$  NPs for each dye.

hindrance for the insertion of the dye through the micellar structure to reach the  $\text{TiO}_2$  NP surface. Analysis of the calculated molecular structure for the dyes supports this interpretation, indicating that the largest molecular dimension (D) across the perylenes' bay substituents varies in the series as  $D1$  (9 Å) <  $D2$  (13 Å) <  $D3$  (27 Å); see Figure S3b in the Supporting Information.

**Steady State Absorption and Emission Spectra and Emission Anisotropy.** Steady state fluorescence anisotropy measurements were performed to gain insight on the location of the dyes in micellar suspensions. Table 2 shows that the fluorescence anisotropy of **1**, **2**, and **3** is considerably higher in micellar suspensions than in the low viscosity solvent THF, indicating that the movement of the dye is significantly restricted and suggesting that it is preferentially located in the ordered micellar environment. This preferential location of the

**Table 2.** Steady State Fluorescence Anisotropy ( $r$ ) of Perylene Dyes in Different Environments<sup>a</sup>

	THF	micelle	micelle/ $\text{TiO}_2$
<b>1</b>	0.004 (0.002)	0.12 (0.01)	0.24 (0.01)
<b>2</b>	0.011 (0.001)	0.15 (0.02)	0.33 (0.03)
<b>3</b>	0.015 (0.007)	0.04 (0.01)	0.21 (0.01)

<sup>a</sup>Anisotropy was measured in an L-format geometry spectrofluorimeter. The reported numbers are the average and the standard deviation (in parentheses) of the values obtained over the 520–610, 710–770, and 550–640 nm spectral ranges for **1**, **2**, and **3**, respectively.

dye generates a relatively high local concentration of the dye in the micellar environment which presumably facilitates the binding of dye to the adjacent oxide surface in solutions of micelles with  $\text{TiO}_2$  NPs. Under these conditions, the fluorescence of **1** and **2** in the  $\text{TiO}_2$ –micelle suspension is highly reduced (~70% quenched for **1**- $\text{TiO}_2$  and **2**- $\text{TiO}_2$  compared to the corresponding control samples without  $\text{TiO}_2$ ). In the case of the **1**- $\text{TiO}_2$  system, the emission is dominated by the spectrum of the closed anhydride species of the dye (Scheme 1, C), while the absorption spectrum has a major contribution corresponding to the open bound species (OB). The lack of significant emission corresponding to the OB species suggests an efficient fluorescence deactivation pathway by electron injection from photoexcited dye into the  $\text{TiO}_2$  conduction band (see Scheme 2). The remaining emission of the **1**- $\text{TiO}_2$  system, which is presumably from the nonbound C species located in the micellar environment, is more polarized than that of **1** in the micelle without  $\text{TiO}_2$ . This indicates that the  $\text{TiO}_2$  NP restricts the movement of the nonbound dye presumably by creating a more rigid micelle due to the strong electrostatic interaction of the positively charged  $\text{TiO}_2$  surface and the negatively charged sulfonate group of the surfactant. Similar observations were found for the **2**- $\text{TiO}_2$  system, although it is difficult to discriminate the contribution of the C species and partially OB species due to the relatively small spectral shift in their emission spectra. The shape of the fluorescence excitation spectra of the **2**- $\text{TiO}_2$  system is in between the absorption spectra of the **2**- $\text{TiO}_2$  and **2**-micelle systems, indicating a significant contribution of both the C and OB species to the observed fluorescence. In the case of the **3**- $\text{TiO}_2$  system, the emission spectrum is dominated by the emission of the C species and the steady state emission anisotropy measurements in different environments show similar trends to the other perylene systems, but not so marked. This observation is consistent with the dye being located in the outer layer of the micellar structure but not close enough to attach to the  $\text{TiO}_2$  surface.

**Time Resolved Fluorescence Anisotropy.** Figure 6 shows the fluorescence anisotropy decays of dyes **1**, **2**, and **3** in different environments. The fluorescence anisotropy decay of **1** in heptane can be fitted with one fast decay lifetime of 81 ps. However, when **1** is dissolved in a micelle solution (control sample), the anisotropy shows a biexponential decay with components of 81 ps (2%) and 1.67 ns (98%). The 81 ps component is associated to the rotational correlation time of **1** in the heptane, whereas the 1.67 ns component could be associated to the rotation of the dye within the surfactant layer of the micelle. Alternatively, the 1.67 ns component can be associated to the rotation of the whole dye–micelle assembly (the decay closely matches the rotational correlation time of a sphere with a diameter of ~3.5 nm in hexane).<sup>83</sup> The

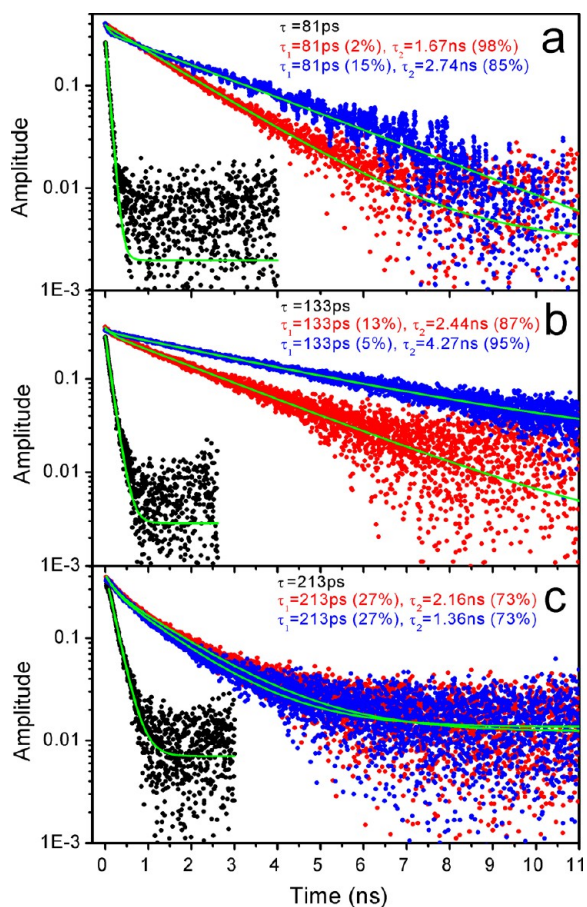


**Figure 6.** (a) Fluorescence anisotropy decays (data points) of **1** in heptane (black), micelle solution (red), and  $\text{TiO}_2$ -micelle solution (blue). Smooth lines show exponential fits to the data. Samples were excited and emission collected at the following wavelengths: heptane and micelle:  $\lambda_{\text{ex}} = 520 \text{ nm}$ ,  $\lambda_{\text{em}} = 600 \text{ nm}$ ;  $1\text{-TiO}_2$ :  $\lambda_{\text{ex}} = 420 \text{ nm}$ ,  $\lambda_{\text{em}} = 510 \text{ nm}$ . (b) Same as part a but for dye **2**. Heptane:  $\lambda_{\text{ex}} = 640 \text{ nm}$ ,  $\lambda_{\text{em}} = 750 \text{ nm}$ ; micelle:  $\lambda_{\text{ex}} = 640 \text{ nm}$ ,  $\lambda_{\text{em}} = 750 \text{ nm}$ ;  $2\text{-TiO}_2$ :  $\lambda_{\text{ex}} = 640 \text{ nm}$ ,  $\lambda_{\text{em}} = 750 \text{ nm}$ . (c) Same as part a but for dye **3**. Heptane, micelle, and  $3\text{-TiO}_2$ :  $\lambda_{\text{ex}} = 515 \text{ nm}$  and  $\lambda_{\text{em}} = 600 \text{ nm}$ . The dye concentration was  $\sim 10^{-6} \text{ M}$  for all samples.

anisotropy decay of **1** in a micelle solution containing  $\text{TiO}_2$  NPs shows a biexponential decay with a 81 ps (15%) component associated with the free dye in heptane and a longer 2.74 ns (85%) component associated with the rotation of the dye in the restricted surfactant layer or with the rotation of the whole  $1\text{-TiO}_2/\text{micelle}$  assembly in heptane. Dye **2** shows analogous behavior with slightly larger decay components in all media; this difference is associated with the larger molecular dimension *D* (see Figure S3b, Supporting Information) of **2** vs **1** which hinders the rotation of **2** relative to that of **1**. Dye **3** dissolved in heptane and micelles shows analogous behavior to **1** and **2** but with slightly larger decay components consistent with a larger steric hindrance for rotation due to the bulky *t*-butylphenoxy groups. The anisotropy decay of **3** in micelles with  $\text{TiO}_2$  NPs is very similar to that in micelles without NPs. This observation is consistent with the lack of spectroscopic evidence for opening of the anhydride groups and putative binding to the  $\text{TiO}_2$  surface. Overall, the analysis of the time-resolved data shows results in line with those of the steady state anisotropy emission shown in Table 2.

**Time Resolved Emission.** TC-SPC measurements were performed to investigate the nature of the steady state emission quenching observed for the dye- $\text{TiO}_2$  systems. Figure 7a

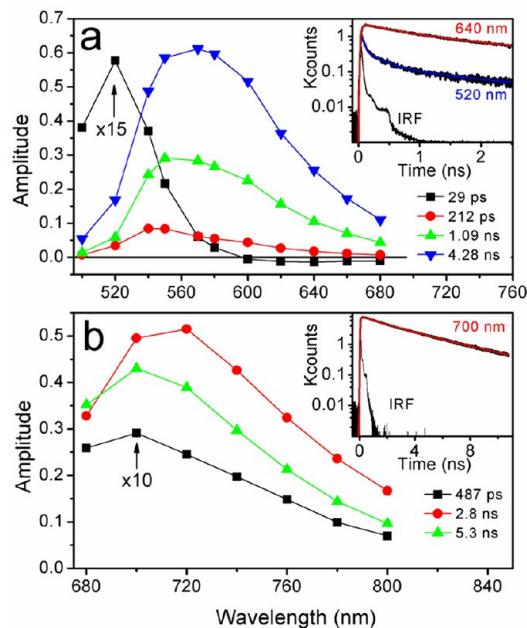


**Figure 7.** (a) Fluorescence decay associated spectra of the  $1\text{-TiO}_2$  system; data was acquired with excitation at 480 nm. Data was globally fitted ( $\chi^2 = 1.14$ ) as described in the experimental section. Inset: kinetic traces and corresponding fits (smooth line) at selected wavelengths and the instrument response function (IRF). (b) Same as part a for the  $2\text{-TiO}_2$  system ( $\chi^2 = 1.10$ ). Data was acquired with excitation at 640 nm. The short-lived components were multiplied by a factor to make them clearly visible.

shows the fluorescence decay associated spectra (DAS) of the  $1\text{-TiO}_2$  system. Global analysis of kinetics yields four decay components ( $\chi^2 = 1.14$ ) with lifetimes of 29 ps, 212 ps, 1.09 ns, and 4.28 ns. To a first approximation, the 29 ps component with maximum at 520 nm is associated with the **1-OB** (open bound species) and the rest of the components are associated with the **1-C** (closed unbound species) in different environments. On the basis of these assignments, the first fluorescence DAS (29 ps) shows energy transfer from **1-OB** (open bound species) to **1-C**, as indicated by the negative amplitude above 600 nm. The second (212 ps) and third (1.09 ns) components show energy migration in between **1-C** species which are in slightly different environments toward the most solvated one, with the lowest energy (4.28 ns component). Overall, the data indicates the existence of a nonhomogeneous system with several dyes per micelle. Analogous measurements on the  $1\text{-micelle}$  system (control sample without  $\text{TiO}_2$  NPs) show longer lived multiexponential decays (see Figure S4a in the Supporting Information) consistent with the high emission quenching observed for  $1\text{-TiO}_2$  vs  $1\text{-micelle}$  in the steady state measurements (*vide supra*).

Figure 7b shows the fluorescence decay associated spectra (DAS) of the  $2\text{-TiO}_2$  system. Global analysis yields four decay components ( $\chi^2 = 1.10$ ) with lifetimes of 487 ps, 2.8 ns, and 5.3 ns. The 487 ps component is associated with the **2-OB** (partially open bound species) and could be assigned in principle to the photoinduced electron injection process from **2-OB** to  $\text{TiO}_2$ . However, some electron injection may occur

faster than the instrument resolution ( $\sim 10$  ps) and therefore is non-time-resolved in this experiment. The rest of the components are associated with the 2-C (closed nonbound species) in different environments. Analogous measurements on the 2-micelle system (control sample without  $\text{TiO}_2$  NPs) show a longer lived biexponential decay (2.9 and 4.9 ns, see Figure S4b in the Supporting Information) consistent with the high emission quenching observed for 2- $\text{TiO}_2$  vs 2-micelle in the steady state measurements (*vide supra*).

**Time Resolved Absorption.** Femtosecond pump–probe experiments were performed to establish the kinetics of the photoinduced electron transfer reaction of the dye– $\text{TiO}_2$  system. Figure 8a shows the results for the 1- $\text{TiO}_2$  system;

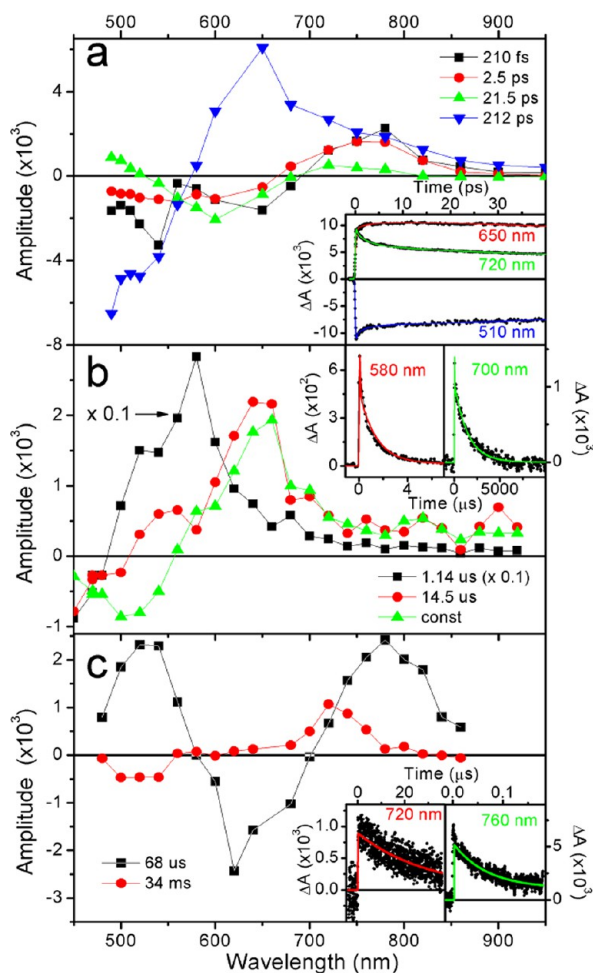


**Figure 8.** (a) Decay associated spectra of the 1- $\text{TiO}_2$  system measured by pump–probe (fs to ps range). Data was acquired with laser excitation at 460 nm. Inset: kinetic traces (data points) and corresponding fits (smooth lines) at selected wavelengths. (b) Same as part a but measured by flash photolysis (ns to  $\mu$ s range). Data was acquired with laser excitation at 440 nm. (c) Decay associated spectra of the 2- $\text{TiO}_2$  system in argon saturated solution measured by flash photolysis (ns to  $\mu$ s range). Data was acquired with laser excitation at 660 nm.

global analysis of kinetics (measured up to 40 ps time delay) shows four decay components with lifetimes of 210 fs, 2.5 ps, 21.5 ps, and 212 ps. The 40 ps time window used in the experiment was chosen to accurately determine the faster components of the decay; the 212 ps component cannot be accurately determined with this window and was fixed in the

analysis based on the information provided by the TC-SPC experiments (*vide supra*). The decay associated spectra (DAS) of the 210 fs component can be attributed to the formation of a charge transfer state between 1-OB and  $\text{TiO}_2$  (i.e.,  $1^{*+}\text{-TiO}_2(\text{e}^-)$ ). It shows decay of stimulated emission and singlet excited state absorption at  $\sim 540$  and 780 nm, respectively, and formation (negative amplitude) of 1-OB radical cation with characteristic absorption at  $\sim 650$  nm.<sup>75,109</sup> The DAS of the 2.5 ps component can be attributed to the decay of 1-C, showing ground state bleaching and stimulated emission at  $\sim 500$ –700 nm and singlet excited state absorption at  $\sim 780$  nm. This DAS can be associated with the process seen in the fluorescence decays, i.e., energy migration in between 1-C species in different environments. The 21.5 ps component is most likely due to the energy transfer process between 1-OB and 1-C, as seen in the fluorescence decay data (Figure 7a, 29 ps fluorescence DAS). The DAS of the 212 ps component shows a mixture of two main processes: (a) decay of singlet excited state of the 1-C species (as seen in the fluorescence decay data) and (b) decay of the  $1^{*+}\text{-TiO}_2(\text{e}^-)$  charge separated state with strong absorption at  $\sim 650$  nm and weak absorption around 850–1000 nm characteristic of the 1-OB<sup>75,109</sup> radical cation species and free carrier (injected electrons) in the  $\text{TiO}_2$  semiconductor,<sup>110</sup> respectively.

Transient absorption measurements on the 1- $\text{TiO}_2$  system in the nanosecond to millisecond time range were performed to complement the pump–probe data on the faster time scale; the results are shown in Figure 8b. Global analysis of the kinetics shows three decay components: 1.14  $\mu$ s, 14.5  $\mu$ s, and a component that does not decay within the 40 ms time window. The 1.14  $\mu$ s DAS is associated with the decay of triplet excited states of 1-C and 1-OB showing transient absorption in the  $\sim 500$ –650 nm range and ground state bleaching at 450 and 510 nm. The other two DAS are associated with the decay of the  $1^{*+}\text{-TiO}_2(\text{e}^-)$  state. They show the characteristic ground state bleaching and induced absorption seen in the pump–probe data (see Figure 8a, 212 ps DAS). The nondecaying transient has ground state bleaching at  $\sim 510$  nm and is associated with the charge transfer state formed with 1-C most likely due to migration of charge from 1-OB to 1-C. The triplet excited state is not clearly shown in these measurements, since it is most likely quenched due to the presence of molecular oxygen. To determine the lifetime of the nonresolved component, a kinetic trace at 700 nm was recorded up to 10 ms; see the Figure 8b inset. Fitting of this trace yields two decay components of  $\sim 15$   $\mu$ s and  $\sim 1.5$  ms. As mentioned before, both of these components are consistent with the decay of  $1^{*+}$  species.

Flash photolysis measurements on the 2- $\text{TiO}_2$  system in argon saturated solution are shown in Figure 8c. Global fit to the data yields two components: a long-lived component of 34 ms assigned to the decay of the  $2^{*+}\text{-TiO}_2(\text{e}^-)$  charge transfer state and a 68  $\mu$ s DAS assigned to 2-OB and 2-C triplet states. Measurements in air saturated solutions (see Figure S5 in the Supporting Information) show only one DAS of 30 ms assigned to the  $2^{*+}\text{-TiO}_2(\text{e}^-)$  state with spectral features very similar to the long decay measured in argon. The transients in the 520–700 and 640–820 nm regions correspond to the 2-OB ground state absorption recovery and the 2-OB radical cation absorption decay, respectively.

Attempts to determine the formation rate of  $2^{*+}\text{-TiO}_2(\text{e}^-)$  at short time scales using the pump–probe technique showed only features associated with the excited state decay (see Figure

S6, Supporting Information). The lack of radical cation absorption at early times is probably due to the long lifetime of the  $2^{\bullet+}\text{-TiO}_2(\text{e}^-)$  state which precludes the recovery of the  $2\text{-TiO}_2$  system ground state in the time between laser pulses (2 ms, pulse frequency = 500 Mz) coupled to slow sample mixing due to the high viscosity of the solutions.

Rigorous analysis of time-resolved emission and absorption data in a non-homogeneous system requires the use of a model which considers a distribution of exponential decays to describe the kinetics of each transient species. The distribution of decays accounts for the distribution of available environments in the heterogeneous system. In our analysis, we used the minimum number of exponential components that adequately fitted the experimental data within the experimental error. Thus, it is likely that the reported decay components correspond to a weighted mean value of the actual distribution of constants associated with each species.

**Distribution of Dyes in the Micellar Solution.** To better understand the dye– $\text{TiO}_2$  assembly process, it is useful to discuss the expected distribution of dyes in micellar systems. The distribution of nonreacting dyes (i.e., in anhydride form) in a micelle microemulsion can be calculated from the concentration of dye and micelles ( $C_{\text{dye}}$  and  $C_{\text{m}}$ , respectively) assuming Poisson statistics,<sup>111</sup> as shown in eq 4:

$$P_n = \frac{\lambda^n e^{-\lambda}}{n!} \quad (4)$$

where  $P_n$  is the probability of finding  $n$  dyes in a given micelle and  $\lambda_{\text{m}} = C_{\text{dye}}/C_{\text{m}}$  is the average number of dyes per micelle. In our experiments,  $\lambda_{\text{m}} > 10^{-3}$  (see the Supporting Information); thus, the probability of finding two (or more) dyes in a given micelle is less than one in a million. On the other hand, considering that  $\lambda_{\text{NP}} = C_{\text{dye}}/C_{\text{NP}} \sim 0.77$  (see the Supporting Information) and assuming that the dyes are distributed exclusively among micelles that contain  $\text{TiO}_2$  NPs, the probability of finding two and three dyes per NP are  $P_2 \sim 0.14$  and  $P_3 \sim 0.03$ , respectively. Comparison of  $C_{\text{m}} \sim 10^{-3}$  M and  $C_{\text{NP}} \sim 1.3 \times 10^{-6}$  indicates that in the  $\text{TiO}_2$ –NP microheterogeneous solutions a large fraction of the total micelles does not contain  $\text{TiO}_2$  NPs. The results of these calculations and the evidence for dye aggregation shown in the time-resolved experiments (*vide supra*) suggest that in the equilibrated  $1\text{-TiO}_2$  and  $2\text{-TiO}_2$  systems the dyes are preferentially located in the small fraction of the micelles that contain  $\text{TiO}_2$  NPs rather than being statistically distributed among all the available micelles. This preferential dye location can be explained considering the following mechanism. At early times after dye addition, the dyes are statistically distributed among all the available micelles in the solution by micelle–collision mediated dye exchange. When a dye reaches a micelle containing a  $\text{TiO}_2$  NP, it can attach to the oxide surface and it is longer available to be exchanged with other micelles on subsequent collisions. Eventually, all nonbound dyes “find” micelles containing a  $\text{TiO}_2$  NP and attach to them. The slow equilibration process shown in Figure 4a,b could in principle be evidence of the proposed mechanism.

**Photoinduced Electron Transfer.** The spectroscopic results discussed above show evidence that both the  $1\text{-TiO}_2$  and  $2\text{-TiO}_2$  systems undergo photoinduced electron transfer to yield the dye– $\text{TiO}_2$  charge separated state. Global analysis of pump–probe and flash photolysis results indicate that the apparent forward and backward rate constants for the formation and

decay of the  $1^{\bullet+}\text{-TiO}_2(\text{e}^-)$  state are  $k_{\text{F}} \sim 4.8 \times 10^{12} \text{ s}^{-1}$  (1/210 fs) and  $k_{\text{B}} < 6.9 \times 10^4 \text{ s}^{-1}$  (1/14.5  $\mu\text{s}$ ), respectively. On the other hand, as it was mentioned above, it was not possible to measure by pump–probe the  $k_{\text{F}}$  of the  $2^{\bullet+}\text{-TiO}_2(\text{e}^-)$ . TC-SPC results for this system show a fluorescence decay with relatively slow components; the shortest decay component of  $\sim 490$  ps for  $2^{\bullet+}\text{-TiO}_2$  might in principle be associated with the formation of the  $2^{\bullet+}\text{-TiO}_2(\text{e}^-)$ ; however, due to the limited time resolution of the TC-SPC experiment, there is most likely a much faster unresolved fluorescence decay component associated with photoinduced electron injection on a shorter time scale ( $< 10$  ps). Formation of  $2^{\bullet+}\text{-TiO}_2(\text{e}^-)$  was confirmed by flash photolysis experiments showing clear features of charge separated state that decayed on a very long time scale,  $k_{\text{b}} = 33 \text{ s}^{-1}$  (1/30 ms). For the  $3\text{-TiO}_2$  system, the spectroscopic studies indicate that the dye does not bind to the  $\text{TiO}_2$  NPs and show no evidence of photoinduced electron injection. Thus, in the following analysis only, the  $1\text{-TiO}_2$  and  $2\text{-TiO}_2$  systems will be considered.

The experimentally determined electron transfer rate constants can be discussed in terms of eq 5 and similar equations that have been developed to describe electron transfer from a single donating state to a continuum of accepting states, such as those present in the conduction band of  $\text{TiO}_2$  nanoparticles.<sup>1,98,112–115</sup>

$$k_{\text{F}(\text{eT})} = \frac{2\pi}{\hbar} \int_{-\infty}^{\infty} \rho(E) (1 - f(E)) |\bar{H}(E)|^2 (4\pi\lambda k_{\text{B}}T)^{-1/2} e^{-(\lambda + \Delta G^0 + E)^2 / 4\lambda k_{\text{B}}T} dE \quad (5)$$

where  $\rho(E)$  is the effective density of states at the energy  $E$  relative to the conduction band edge,  $f(E)$  represents the Fermi distribution function,  $\bar{H}(E)$  is the average electronic coupling between the dye excited state and all  $k$  states in the semiconductor, and  $\lambda$  is the total reorganization energy.  $\Delta G^0$  is the energy difference between the energy level of the excited dye and the bottom of the conduction band and can be written as  $\Delta G^0 = E_{\text{CB}} - E(\text{D}^+/\text{D}^*)$ . To a first approximation,  $\bar{H}(E)$  and  $\lambda$  are assumed to be the same for all the dye– $\text{TiO}_2$  systems given the analogous structure of the dyes and their expected identical binding modes to the  $\text{TiO}_2$  surface. Under these approximations and given that  $E(2^+/2^*) > E(1^+/1^*)$ , the rate constants for forward electron transfer are expected to follow the relationship  $k_{\text{F}}(2) > k_{\text{F}}(1)$ . The previous analysis suggests that the  $\sim 490$  ps fluorescence quenching component seen on the  $2\text{-TiO}_2$  system is not due to the formation of the  $2^{\bullet+}\text{-TiO}_2(\text{e}^-)$  state and that  $k_{\text{F}}(2) > 4.8 \times 10^{12} \text{ s}^{-1}$ .

Models for  $k_{\text{B}}$  generally involve semiconductor effects such as charge trapping and transport which are not well-defined in our system, so no detailed analysis will be carried out for this case. It is noteworthy to mention that approaches entirely based on quantum-chemical calculations can be used to estimate dye– $\text{TiO}_2$  electron injection times.<sup>76,116</sup> Such methods have been successfully applied to the study of perylene– $\text{TiO}_2$  systems with phosphonic and carboxylic acid anchoring groups and various spacer groups<sup>76</sup> and will therefore be interesting to apply to the systems described in this work.

## CONCLUSIONS

We report the successful sensitization of  $\text{TiO}_2$  nanoparticles inside reverse micelles by perylene dyes. These systems having well dispersed oxide nanoparticles of small diameter ( $< 5$  nm) spherical shape and relative narrow size distribution are good

models for the study of dye–semiconductor photoinduced electron transfer reactions in solution. Steady state and transient absorption and emission spectroscopy indicate that perylenes **1** and **2** efficiently attach to TiO<sub>2</sub> nanoparticles inside reverse micelles. The binding of the dyes to the oxide surface involves the attachment of dicarboxylic acid groups produced by hydrolysis of a cyclic anhydride. Binding of perylene **3** to the NPs was inefficient presumably due to steric hindrance resulting from the bulky *t*-butylphenoxy groups connected at bay positions of the dye. The 1-TiO<sub>2</sub> and 2-TiO<sub>2</sub> systems undergo fast photoinduced electron transfer ( $k_f < 210$  fs) to form the dye<sup>•+</sup>–TiO<sub>2</sub>(e<sup>-</sup>) charge separated state. The electron injected into the semiconductor NP recombines with the dye radical cation on a very long time scale ( $k_b(\mathbf{1}) > 14$   $\mu$ s and  $k_b(\mathbf{2}) = 30$  ms).

It is clear from these observations that the molecular structure of the dye plays an important role in the phenomena we observed. In principle, it should be possible to use dyes with the required substitutions to target specific regions of micro-heterogeneous media; it is also possible to modulate the redox potential of the dyes and thereby control electron injection. Therefore, one could use these design parameters to envision applications of molecular systems to sensitize semiconductor nanoparticles located in specific regions of a micro-heterogeneous environment. Additionally, one could imagine other applications in which the dyes are used to map complex landscapes by means of their fluorescence.

## ■ ASSOCIATED CONTENT

### ■ Supporting Information

Figures S1–S6 and description for the estimation of the average number of dyes per micelle and per TiO<sub>2</sub> NP. This material is available free of charge via the Internet at <http://pubs.acs.org>.

## ■ AUTHOR INFORMATION

### ■ Corresponding Author

\*E-mail: [rpalacios@exa.unrc.edu.ar](mailto:rpalacios@exa.unrc.edu.ar).

### ■ Notes

The authors declare no competing financial interest.

## ■ ACKNOWLEDGMENTS

This work has been supported in part by grants from the Agencia Nacional de Promoción Científica y Tecnológica (ANPCyT), Argentina (PICT 140/08, 2213/07, 2691/11, and PRH23 PME01); the Consejo Nacional de Investigaciones Científicas y Técnicas (CONICET), Argentina (PIP 11220090100839/10, 11220100100284/11, and CIAM/09); the Secretaría de Ciencia y Técnica, UNRC Argentina; the Ministerio de Ciencia y Tecnología Córdoba, Argentina (PID 2010); the National Science and Engineering Research Council (Canada) and a Tomlinson Award, McGill University; the National Science Foundation, USA (DMR-0908656); and the Consejo Nacional de Ciencia y Tecnología, México (CIAM-2008-101939). R.E.P., C.A.C., and S.B. are permanent research staff of CONICET. The research of L.I.H. was supported by the ANPCyT through a Ph.D. scholarship. R.G. thanks the NSERC of Canada for a postgraduate scholarship. D.D.M.-H. is supported by the National Science Foundation Graduate Research Fellowship Program (NSF-GRFP) under Grant No. DGE-0802261 and by the More Graduate Education at Mountain States Alliance (MGE@MSA) Alliance for Graduate Education and the Professoriate (AGEP) National Science

Foundation (NSF) Cooperative Agreement No. HRD-0450137. R.E.P. thanks the CSACS of McGill University for a visiting professor scholarship. R.E.P. thanks Juan Palacios for his generous donation of optical components used in this work.

## ■ REFERENCES

- (1) Anderson, N. A.; Lian, T. Q. *Annu. Rev. Phys. Chem.* **2005**, *56*, 491–519.
- (2) Argazzi, R.; Iha, N. Y. M.; Zabri, H.; Odobel, F.; Bignozzi, C. A. *Coord. Chem. Rev.* **2004**, *248*, 1299–1316.
- (3) Neouze, M. A.; Schubert, U. *Monatsh. Chem.* **2008**, *139*, 183–195.
- (4) Stipkala, J. M.; Castellano, F. N.; Heimer, T. A.; Kelly, C. A.; Livi, K. J. T.; Meyer, G. J. *Chem. Mater.* **1997**, *9*, 2341–2353.
- (5) Zhang, J. Z. *J. Phys. Chem. B* **2000**, *104*, 7239–7253.
- (6) Zhang, Y. Y.; Galoppini, E. *ChemSusChem* **2010**, *3*, 410–428.
- (7) Clifford, J. N.; Martinez-Ferrero, E.; Viterisi, A.; Palomares, E. *Chem. Soc. Rev.* **2011**, *40*, 1635–1646.
- (8) Gratzel, M. J. *Photochem. Photobiol., C* **2003**, *4*, 145–153.
- (9) Gratzel, M. *Acc. Chem. Res.* **2009**, *42*, 1788–1798.
- (10) Hagfeldt, A.; Boschloo, G.; Sun, L. C.; Kloo, L.; Pettersson, H. *Chem. Rev.* **2010**, *110*, 6595–6663.
- (11) Hagfeldt, A.; Gratzel, M. *Acc. Chem. Res.* **2000**, *33*, 269–277.
- (12) Listorti, A.; O'Regan, B.; Durrant, J. R. *Chem. Mater.* **2011**, *23*, 3381–3399.
- (13) Escalada, J. P.; Pajares, A.; Gianotti, J.; Massad, W. A.; Bertolotti, S.; Amat-Guerri, F.; Garcia, N. A. *Chemosphere* **2006**, *65*, 237–244.
- (14) Henderson, M. A. *Surf. Sci. Rep.* **2011**, *66*, 185–297.
- (15) Jin, Z. L.; Zhang, X. J.; Lu, G. X.; Li, S. B. *J. Mol. Catal. A: Chem.* **2006**, *259*, 275–280.
- (16) Kamat, P. V. *Prog. React. Kinet.* **1994**, *19*, 277–316.
- (17) Kumar, S. G.; Devi, L. G. *J. Phys. Chem. A* **2011**, *115*, 13211–13241.
- (18) Pei, D. H.; Luan, J. F. *Int. J. Photoenergy* **2012**, DOI: 10.1155/2012/262831.
- (19) Beltran-Perez, G.; Lopez-Huerta, F.; Munoz-Aguirre, S.; Castillo-Mixcoatl, J.; Palomino-Merino, R.; Lozada-Morales, R.; Portillo-Moreno, O. *Sens. Actuators, B* **2006**, *120*, 74–78.
- (20) Stux, A. M.; Meyer, G. J. *J. Fluoresc.* **2002**, *12*, 419–423.
- (21) Tokudome, H.; Yamada, Y.; Sonezaki, S.; Ishikawa, H.; Bekki, M.; Kanehira, K.; Miyauchi, M. *Appl. Phys. Lett.* **2005**, *87*, No. 213901.
- (22) Yimit, A.; Itoh, K.; Murabayashi, M. *Sens. Actuators, B* **2003**, *88*, 239–245.
- (23) Yusoff, N. H.; Salleh, M. M.; Yahaya, M. *Sains Malays.* **2008**, *37*, 249–253.
- (24) Gundlach, L.; Ernstorfer, R.; Willig, F. *Prog. Surf. Sci.* **2007**, *82*, 355–377.
- (25) Hilgendorff, M.; Sundström, V. *J. Phys. Chem. B* **1998**, *102*, 10505–10514.
- (26) Katoh, R.; Furube, A.; Barzykin, A. V.; Arakawa, H.; Tachiya, M. *Coord. Chem. Rev.* **2004**, *248*, 1195–1213.
- (27) Prezhdo, O. V.; Duncan, W. R.; Prezhdo, V. V. *Acc. Chem. Res.* **2008**, *41*, 339–348.
- (28) Stergiopoulos, T.; Bernard, M. C.; Goff, A. H. L.; Falaras, P. *Coord. Chem. Rev.* **2004**, *248*, 1407–1420.
- (29) Bell, T. D. M.; Pagba, C.; Myahkostupov, M.; Hofkens, J.; Piotrowski, P. *J. Phys. Chem. B* **2006**, *110*, 25314–25321.
- (30) Durrant, J. R.; Haque, S. A.; Palomares, E. *Coord. Chem. Rev.* **2004**, *248*, 1247–1257.
- (31) Haque, S. A.; Palomares, E.; Cho, B. M.; Green, A. N. M.; Hirata, N.; Klug, D. R.; Durrant, J. R. *J. Am. Chem. Soc.* **2005**, *127*, 3456–3462.
- (32) Tachibana, Y.; Nazeeruddin, M. K.; Gratzel, M.; Klug, D. R.; Durrant, J. R. *Chem. Phys.* **2002**, *285*, 127–132.
- (33) Anandan, S.; Yoon, M. *Spectrochim. Acta, Part A* **2004**, *60*, 885–888.
- (34) Chen, C.; Qi, X.; Zhou, B. *J. Photochem. Photobiol., A* **1997**, *109*, 155–158.

- (35) He, J.; Chen, F.; Zhao, J.; Hidaka, H. *Colloids Surf., A* **1998**, *142*, 49–57.
- (36) He, J.; Zhao, J.; Shen, T.; Hidaka, H.; Serpone, N. *J. Phys. Chem. B* **1997**, *101*, 9027–9034.
- (37) Huang, H.; Zhou, J.; Zhou, Y.; Zhou, Y.; Feng, Y. *Int. J. Photoenergy* **2010**, *2010*, 1–5.
- (38) Huber, R.; Moser, J. E.; Grätzel, M.; Wachtveitl, J. *Chem. Phys.* **2002**, *285*, 39–45.
- (39) Joselevich, E.; Willner, I. *J. Phys. Chem.* **1994**, *98*, 7628–7635.
- (40) Kamat, P. V.; Chauvet, J. P.; Fessenden, R. W. *J. Phys. Chem.* **1986**, *90*, 1389–1394.
- (41) Kamat, P. V.; Fox, M. A. *Chem. Phys. Lett.* **1983**, *102*, 379–384.
- (42) Kathiravan, A.; Anbazhagan, V.; Asha Jhonsi, M.; Renganathan, R. *Spectrochim. Acta, Part A* **2008**, *70*, 615–618.
- (43) Kathiravan, A.; Chandramohan, M.; Renganathan, R.; Sekar, S. *Spectrochim. Acta, Part A* **2009**, *71*, 1783–1787.
- (44) Kathiravan, A.; Chandramohan, M.; Renganathan, R.; Sekar, S. *Spectrochim. Acta, Part A* **2009**, *72*, 496–501.
- (45) Kathiravan, A.; Kumar, P. S.; Renganathan, R.; Anandan, S. *Colloids Surf., A* **2009**, *333*, 175–181.
- (46) Kathiravan, A.; Renganathan, R. *Spectrochim. Acta, Part A* **2008**, *71*, 1106–1109.
- (47) Kathiravan, A.; Renganathan, R. *Spectrochim. Acta, Part A* **2008**, *71*, 1080–1083.
- (48) Kathiravan, A.; Renganathan, R. *J. Colloid Interface Sci.* **2009**, *331*, 401–407.
- (49) Moser, J.; Graetzel, M. *J. Am. Chem. Soc.* **1984**, *106*, 6557–6564.
- (50) Prashant V, K. *J. Photochem.* **1985**, *28*, 513–524.
- (51) Qu, P.; Zhao, J.; Zang, L.; Shen, T.; Hidaka, H. *Colloids Surf., A* **1998**, *138*, 39–50.
- (52) Rath, M. C.; Palit, D. K.; Mukherjee, T.; Ghosh, H. N. *J. Photochem. Photobiol., A* **2009**, *204*, 209–216.
- (53) Sant, P. A.; Kamat, P. V. *Phys. Chem. Chem. Phys.* **2002**, *4*, 198–203.
- (54) Walters, K. A.; Gaal, D. A.; Hupp, J. T. *J. Phys. Chem. B* **2002**, *106*, 5139–5142.
- (55) Wang, C.-y.; Liu, C.-y.; Wang, W.-q.; Shen, T. *J. Photochem. Photobiol., A* **1997**, *109*, 159–164.
- (56) Wang, C.-y.; Liu, C.-y.; Wang, Y.; Shen, T. *J. Colloid Interface Sci.* **1998**, *197*, 126–132.
- (57) Wu, T.; Xu, S.-J.; Shen, J.-Q.; Chen, S.; Zhang, M.-H.; Shen, T. *J. Photochem. Photobiol., A* **2000**, *137*, 191–196.
- (58) Zang, L.; Liu, C.-Y.; Ren, X.-M. *J. Photochem. Photobiol., A* **1995**, *88*, 47–51.
- (59) Zang, L.; Qu, P.; Zhao, J.; Shen, T.; Hidaka, H. *Chem. Lett.* **1997**, *26*, 791–792.
- (60) Zhang, H.; Zhou, Y.; Zhang, M.; Shen, T.; Xiang, J.; Feng, J. *J. Colloid Interface Sci.* **2003**, *263*, 669–673.
- (61) Zhou, Z.-X.; Qian, S.-P.; Yao, S.-D.; Zhang, Z.-Y. *Dyes Pigm.* **2001**, *51*, 137–144.
- (62) Zhou, Z.; Qian, S.; Yao, S.; Zhang, Z. *Radiat. Phys. Chem.* **2002**, *65*, 241–248.
- (63) Zuo, P.; Li, C.; Wu, Y.-S.; Ai, X.-C.; Wang, X.-S.; Zhang, B.-W.; Zhang, J.-P. *J. Photochem. Photobiol., A* **2006**, *183*, 138–145.
- (64) Avlasevich, Y.; Li, C.; Mullen, K. *J. Mater. Chem.* **2010**, *20*, 3814–3826.
- (65) Cappel, U. B.; Karlsson, M. H.; Pschirer, N. G.; Eickemeyer, F.; Schöneboom, J.; Erk, P.; Boschloo, G.; Hagfeldt, A. *J. Phys. Chem. C* **2009**, *113*, 14595–14597.
- (66) Edvinsson, T.; Li, C.; Pschirer, N.; Schöneboom, J.; Eickemeyer, F.; Sens, R.; Boschloo, G.; Herrmann, A.; Müllen, K.; Hagfeldt, A. *J. Phys. Chem. C* **2007**, *111*, 15137–15140.
- (67) Ferrere, S.; Gregg, B. A. *New J. Chem.* **2002**, *26*, 1155–1160.
- (68) Ferrere, S.; Zaban, A.; Gregg, B. A. *J. Phys. Chem. B* **1997**, *101*, 4490–4493.
- (69) Fortage, J.; Séverac, M.; Houarner-Rassin, C.; Pellegrin, Y.; Blart, E.; Odobel, F. *J. Photochem. Photobiol., A* **2008**, *197*, 156–169.
- (70) Li, C.; Liu, Z.; Schoneboom, J.; Eickemeyer, F.; Pschirer, N. G.; Erk, P.; Herrmann, A.; Mullen, K. *J. Mater. Chem.* **2009**, *19*, 5405–5415.
- (71) Li, C.; Yum, J.-H.; Moon, S.-J.; Herrmann, A.; Eickemeyer, F.; Pschirer, N. G.; Erk, P.; Schöneboom, J.; Müllen, K.; Grätzel, M.; et al. *ChemSusChem* **2008**, *1*, 573–573.
- (72) Mathew, S.; Imahori, H. *J. Mater. Chem.* **2011**, *21*, 7166–7174.
- (73) Planells, M.; Cespedes-Guirao, F. J.; Forneli, A.; Sastre-Santos, A.; Fernandez-Lazaro, F.; Palomares, E. *J. Mater. Chem.* **2008**, *18*, 5802–5808.
- (74) Shibano, Y.; Umeyama, T.; Matano, Y.; Imahori, H. *Org. Lett.* **2007**, *9*, 1971–1974.
- (75) Szarko, J. M.; Neubauer, A.; Bartelt, A.; Socaciu-Siebert, L.; Birkner, F.; Schwarzburg, K.; Hannappel, T.; Eichberger, R. *J. Phys. Chem. C* **2008**, *112*, 10542–10552.
- (76) Nilsing, M.; Persson, P.; Lunell, S.; Ojamae, L. *J. Phys. Chem. C* **2007**, *111*, 12116–12123.
- (77) Liu, H. B.; Xu, J. L.; Li, Y. J.; Li, Y. L. *Acc. Chem. Res.* **2010**, *43*, 1496–1508.
- (78) Liu, H. B.; Zuo, Z. C.; Guo, Y. B.; Li, Y. J.; Li, Y. L. *Angew. Chem., Int. Ed.* **2010**, *49*, 2705–2707.
- (79) Zheng, H. Y.; Li, Y. J.; Liu, H. B. A.; Yin, X. D.; Li, Y. L. *Chem. Soc. Rev.* **2011**, *40*, 4506–4524.
- (80) Dubey, R. K.; Efimov, A.; Lemmetyinen, H. *Chem. Mater.* **2011**, *23*, 778–788.
- (81) Kohl, C.; Weil, T.; Qu, J. Q.; Mullen, K. *Chem.—Eur. J.* **2004**, *10*, 5297–5310.
- (82) Crans, D. C.; Levinger, N. E. *Acc. Chem. Res.* **2012**, *45*, 1637–1645.
- (83) Lakowicz, J. R. *Principles of Fluorescence Spectroscopy*, 3rd ed.; Springer: New York, 2006; p 961.
- (84) [www.public.asu.edu/~laserweb/asufit/asufit.html](http://www.public.asu.edu/~laserweb/asufit/asufit.html).
- (85) Rasband, W. S. *ImageJ*; U. S. National Institutes of Health: Bethesda, MD, 1997–2012 (<http://imagej.nih.gov/ij/>).
- (86) Frisch, M. J.; Trucks, G. W.; Schlegel, H. B.; Scuseria, G. E.; Robb, M. A.; Cheeseman, J. R.; Scalmani, G.; Barone, V.; Mennucci, B.; Petersson, G. A.; et al. *Gaussian 09*, revision A.02; Gaussian, Inc.: Wallingford, CT, 2009.
- (87) Fukuda, T.; Homma, S.; Kobayashi, N. *Chem.—Eur. J.* **2005**, *11*, 5205–5216.
- (88) Mack, J.; Asano, Y.; Kobayashi, N.; Stillman, M. J. *J. Am. Chem. Soc.* **2005**, *127*, 17697–17711.
- (89) Mack, J.; Bunya, M.; Lansky, D.; Goldberg, D. P.; Kobayashi, N. *Heterocycles* **2008**, *76*, 1369–1380.
- (90) Clark, A. E.; Qin, C. Y.; Li, A. D. Q. *J. Am. Chem. Soc.* **2007**, *129*, 7586–7595.
- (91) Francl, M. M.; Pietro, W. J.; Hehre, W. J.; Binkley, J. S.; Gordon, M. S.; Defrees, D. J.; Pople, J. A. *J. Chem. Phys.* **1982**, *77*, 3654–3665.
- (92) Harihan, P. C.; Pople, J. A. *Theor. Chim. Acta* **1973**, *28*, 213–222.
- (93) Rassolov, V. A.; Pople, J. A.; Ratner, M. A.; Windus, T. L. *J. Chem. Phys.* **1998**, *109*, 1223–1229.
- (94) Shibano, Y.; Imahori, H.; Adachi, C. *J. Phys. Chem. C* **2009**, *113*, 15454–15466.
- (95) Barone, V.; Cossi, M. *J. Phys. Chem. A* **1998**, *102*, 1995–2001.
- (96) Cossi, M.; Rega, N.; Scalmani, G.; Barone, V. *J. Comput. Chem.* **2003**, *24*, 669–681.
- (97) Weng, Y.-X.; Li, L.; Liu, Y.; Wang, L.; Yang, G.-Z. *J. Phys. Chem. B* **2003**, *107*, 4356–4363.
- (98) Sakata, T.; Hashimoto, K.; Hiramoto, M. *J. Phys. Chem.* **1990**, *94*, 3040–3045.
- (99) Redmond, G.; Fitzmaurice, D. *J. Phys. Chem.* **1993**, *97*, 1426–1430.
- (100) Wang, Y.; Herron, N. *J. Phys. Chem.* **1991**, *95*, 525–532.
- (101) Bawendi, M. G.; Steigerwald, M. L.; Brus, L. E. *Annu. Rev. Phys. Chem.* **1990**, *41*, 477–496.
- (102) Monticone, S.; Tufeu, R.; Kanaev, A. V.; Scolan, E.; Sanchez, C. *Appl. Surf. Sci.* **2000**, *162–163*, 565–570.

- (103) Kaniyankandy, S.; Ghosh, H. N. *J. Mater. Chem.* **2009**, *19*, 3523–3528.
- (104) Vayssieres, L.; Persson, C.; Guo, J. H. *Appl. Phys. Lett.* **2011**, *99*.
- (105) Hegazy, A.; Prouzet, E. *Chem. Mater.* **2012**, *24*, 245–254.
- (106) Yacaman, M. J.; Ascencio, J. A.; Liu, H. B.; Gardea-Torresdey, J. *J. Vac. Sci. Technol., B* **2001**, *19*, 1091–1103.
- (107) Falaras, P. *Sol. Energy Mater. Sol. Cells* **1998**, *53*, 163–175.
- (108) Finnie, K. S.; Bartlett, J. R.; Woolfrey, J. L. *Langmuir* **1998**, *14*, 2744–2749.
- (109) Neubauer, A.; Szarko, J. M.; Bartelt, A. F.; Eichberger, R.; Hannappel, T. *J. Phys. Chem. C* **2011**, *115*, 5683–5691.
- (110) Pankove, J. I. *Optical Processes in Semiconductors*; Dover Publications: Mineola, New York, 2010.
- (111) Atik, S. S.; Thomas, J. K. *J. Am. Chem. Soc.* **1981**, *103*, 3543–3550.
- (112) Stockwell, D.; Yang, Y.; Huang, J.; Anfuso, C.; Huang, Z. Q.; Lian, T. Q. *J. Phys. Chem. C* **2010**, *114*, 6560–6566.
- (113) Gao, Y. Q.; Georgievskii, Y.; Marcus, R. A. *J. Chem. Phys.* **2000**, *112*, 3358–3369.
- (114) Ai, X.; Anderson, N. A.; Guo, J. C.; Lian, T. Q. *J. Phys. Chem. B* **2005**, *109*, 7088–7094.
- (115) Ai, X.; Guo, J. C.; Anderson, N. A.; Lian, T. Q. *J. Phys. Chem. B* **2004**, *108*, 12795–12803.
- (116) Lundqvist, M. J.; Nilsing, M.; Lunell, S.; Akermark, B.; Persson, P. *J. Phys. Chem. B* **2006**, *110*, 20513–20525.